Microstructural Transformation and Tribological Properties of Laser-Cladded FeNiCoCrTi$_{0.5}$-xNbC High-Entropy Alloy-Based Composite Coatings

Ying Zhang[1] · Meng Xiao[2] · Yi-min Zhou[3] · Yi-fu Shen[1]

Abstract Laser-cladded FeNiCoCrTi$_{0.5}$-xNbC (x = 3 wt.%, 6 wt.%, 12 wt.%, and 24 wt.%) high-entropy alloy-based composite coatings (HACCs; donated as C1, C2, C3, and C4, respectively) without pores, cracks, and spherical adhesion are successfully prepared and metallurgically deposited on 45 steel. It is found that the as-prepared composite coatings are mainly composed of body-centered cubic (BCC) solid solution and carbides. The increase of the NbC content in FeNiCoCrTi$_{0.5}$-xNbC promotes the transformation of carbides from TiC to NbC, which causes carbides morphology to change from near spherical to polygonal and the carbides size to undergo a process of first decreasing and then significantly increasing. With the increase of the NbC content, the microhardness and wear resistance of FeNiCoCrTi$_{0.5}$-xNbC first increase and then decrease. An appropriate amount of NbC can help FeNiCoCrTi$_{0.5}$-xNbC HACCs resist friction and effectively protect the substrate. However, excessive NbC increases the local brittleness of FeNiCoCrTi$_{0.5}$-xNbC and deteriorates the wear resistance.

Introduction

Chemical, metallurgy, nuclear, and aerospace industries require a stable operation of mechanical equipment under severe working conditions. According to statistics, more than 80% of mechanical part failures occur due to local surface wear (Ref 1, 2). Almost all moving parts, especially shafts, connecting rods, gears, bolts, experience surface wear because of their long-time operations under alternating loads. Therefore, it is necessary to conduct effective surface treatments on these parts to improve their wear resistance.

In recent years, high-entropy alloys (HEAs; known as complex concentration alloys) containing five or more elements (the content of each component ranges between 5 and 35 at.%) have attracted significant research attention (Ref 3). HEAs consisting of solid solutions have a completely different microstructure in comparison with traditional alloys (Ref 4). Especially, HEAs manifest excellent wear resistance, corrosion resistance, oxidation resistance, and thermal stability (Ref 5–8). Currently, surface modification processes for HEAs mainly include mechanical alloying, magnetron sputtering, and cladding (Ref 9–11). Particularly, coatings prepared by mechanical alloying

✉ Yi-fu Shen
yfshen_nuaa@hotmail.com

1 College of Materials Science and Technology, Nanjing University of Aeronautics and Astronautics (NUAA), Nanjing, People's Republic of China

2 Nanjing Institute of Advanced Laser Technology, Nanjing, People's Republic of China

3 Huitu Technology Co., Ltd., Yancheng, People's Republic of China

become mechanically bonded with substrates with a lower bonding strength and contain a large number of pores (Ref 12). Coatings synthesized by magnetron sputtering are too thin to meet heavy-duty requirements (Ref 13). Cladding technologies, such as laser cladding and plasma cladding, can produce coatings with thicknesses ranging from microns to millimeters. Furthermore, cladded coatings contain fine microstructures and become metallurgically bonded to substrates (Ref 14–18). Qiu et al. (Ref 19) use laser cladding to deposit a series of $Al_2CrFeCoCuTiNi_x$ (x = 0.0, 0.5, 1.0, 1.5, 2.0) high-entropy alloy coatings (HEACs) on Q235 steel. The as-prepared coatings consisting of body-centered cubic (BCC) and face-centered cubic (FCC) solid solutions have high microhardness and good wear resistance. Fang et al. (Ref 20) deposit $FeCoCrNiNb_x$ (x = 0.25, 0.6, 0.8) HEACs on industrial pure titanium TA1ELI by plasma cladding and find that the as-prepared coatings exhibit better wear resistance than industrial pure titanium TA1ELI. Qiu (Ref 21) reports that the laser-cladded CoCrFeNiMo HEAC consisting of FCC and BCC solid solutions and Laves phase has excellent wear resistance. Lin et al. (Ref 22) find that the laser-cladded $FeCoCrNiAlNb_{0.75}$ HEAC deposited on Q235 steel has a microhardness of 773 HV with good wear resistance.

Currently, the researches on cladded HEACs mainly focus on pure HEAs. Thus, very few reports are available on ceramic-reinforced HACCs. Therefore, $FeNiCoCrTi_{0.5}$-xNbC (x = 3 wt.%, 6 wt.%, 12 wt.%, 24 wt.%) HACCs are successfully prepared by laser cladding. The nucleation mechanism, precipitation behavior, evolution kinetics, and hardening effect of carbides precipitated in $FeNiCoCrTi_{0.5}$-xNbC are revealed.

Material and Methods

Materials and Laser Cladding Process

The raw powders shown in Table 1 and Fig. 1 were used to synthesize the $FeNiCoCrTi_{0.5}$-NbC_x (x = 3 wt.%, 6 wt.%,

Table 1. The purity, size and melting point of experimental raw materials [23]

Element	Purity, wt.%	Size, μm	Melting point, °C
Fe	99.50	< 50	1538
Ni	99.50	< 50	1453
Co	99.50	1-2	1495
Cr	99.50	< 50	1857
Ti	99.99	≤ 50	1660
NbC	99.00	1-4	3500

12 wt.%, 24 wt.%) composite powders through a planetary mechanical ball mill at 350 r/min for 3 hours. During synthesis, every 30 minutes of mixing was followed by a pause of 20 minutes. The as-obtained $FeNiCoCrTi_{0.5}$-NbC_x powders were placed in a vacuum drying oven under argon protection for dehumidification at 100 °C, and their XRD patterns after ball milling are displayed in Fig. 2. It is noticeable that no intermetallic compounds or new carbides are formed in the composite powders due to low-energy ball milling.

45 steel with the composition shown in Table 2 was cut into a size of 40 mm × 20 mm × 5 mm and used as the substrate. The 45 steel was ground by sandpapers to remove rust, and the residual oil was removed by ethanol and acetone. To ensure a clean surface, the 45 steel was ultrasonically cleaned in ethanol and then dried in a vacuum drying oven at 60 °C for 3 hours.

$FeNiCoCrTi_{0.5}$-NbC_x composite powder beds with a thickness of 1mm were deposited on the surface of 45 steel by a TruDisk 12003disc solid-state laser equipment (wavelength = 1030 nm) under a laser power of 1300 W, a scanning speed of 6 mm/s, and a spot diameter of 3 mm. Moreover, the distribution of laser intensity follows Gauss's law, and the cladding of $FeNiCoCrTi_{0.5}$-NbC_x was protected by argon with a flow rate of 20 L·min^{-1}.

### Microstructural Characterization

The coatings were cut by wire bond electrode cutting (WEC), and their cross-sectional morphologies were characterized by optical microscopy (OM). A Bruker D8 Advance x-ray diffractometer (XRD) equipped with a copper target was used to identify different phases of the coatings in the 2θ range of 5°–80° with a scanning speed of 1°/min at 30 kV and 20 mA. The microstructure and elemental distribution of the coatings were investigated by a Hitachi Se4800 field-emission scanning electron microscope (FESEM) equipped with a Bruker Quantaxe 400 energy-dispersive spectroscopy (EDS).

Microhardness Measurement and Wear Test

The microhardness at different depths of the coatings (spacing = 0.15mm) in the longitudinal direction was measured using an HXS-1000A microhardness tester under a load of 200 g for 15 s. Five microhardness values were measured at each depth to obtain the exact value. An ML-100 wear tester equipped with a friction pair of 400# metallographic sandpaper was operated to conduct dry sliding friction tests of the coatings at room temperature for 30 min under a load of 10 N with a sliding speed of 60 r/min. Each friction test was performed with new sandpaper. The two-dimensional profile of wear tracks and the
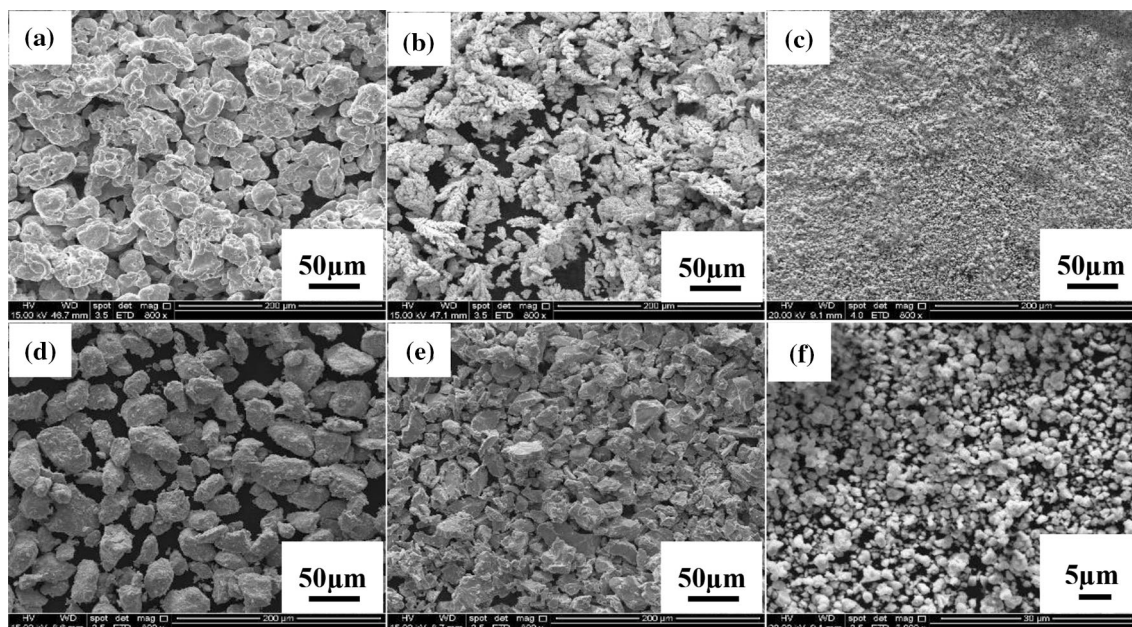
Fig. 1 The morphology of raw powders: (a) Fe, (b) Ni, (c) Co, (d) Cr, (e) Ti, (f) NbC
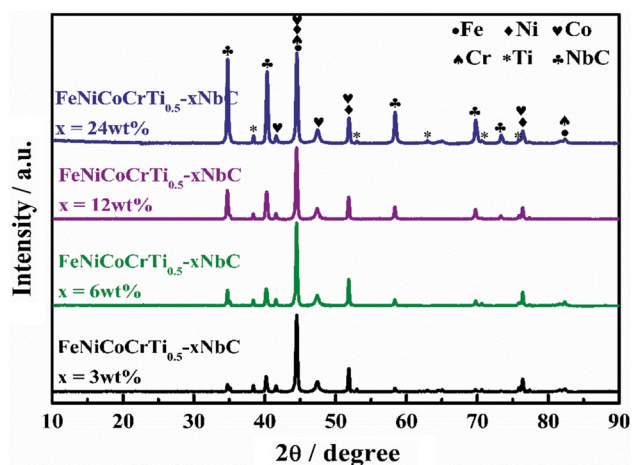
Fig. 2 The XRD patterns of mixed powders after ball milling

roughness of worn surfaces were characterized by a Rtec-3D Profilometer (UP-Dule Mode). Additionally, the volume losses of the coatings after sliding friction were recorded to reflect their wear rates. The worn surface morphologies of the coatings were analyzed by SEM to reveal the wear-resistant mechanism.

Results and Discussion

### Macroscopic Morphology of Cross Section

It is observable from Fig. 3 that the coatings have a hill-shaped morphology without pores and cracks. Moreover,

no spherical adhesion is detected at the edges of the coatings, which can be attributed to the agitation of the laser beam and the convection and mass transfer in the molten pool. As the NbC content increases, clusters and inclusions appear in C4 because certain laser energy is not enough to completely melt the powder. However, each coating is tightly bonded with the substrate, and the EDS line scan results of the coatings and the interfaces are shown in Fig. 4. The distribution curve of each element in the coatings is linear, implying that the distribution of each element is relatively uniform. Simultaneously, the content of each element in the inter-diffusion zone between the coating and the substrate changes continuously and slowly, indicating the formation of a continuous concentration gradient of each element and a good metallurgical bonding at the interface. Evidently, the content of Fe in the coatings is significantly higher than the theoretical value on account of the dilution of substrate. As listed in Fig. 3, the dilution rate first decreases and then increases with the increase of the NbC content. The greater the NbC content, the higher the melting point of the powder bed, which reduces the laser energy that can melt the substrate surface and decreases the dilution rate. Moreover, when the NbC content in the coatings is too high, rapid laser heating generates a strong stress and a large amount of heat accumulation at the interface between NbC and metals due to their different properties, which induces the instability and fluctuation of the molten pool (Ref 24, 25). In addition, gas existing in the molten pool and the powder gap expands and escapes, resulting in a violent reaction with sputtering and the loss of powder during cladding (Ref 26). Thus, the

Table 2. The chemical composition of 45 steel (wt.%)

Element	C	Si	Mn	P	S	Cr	Ni	Fe
Content	0.42-0.45	0.17-0.37	0.50-0.80	≤ 0.035	≤ 0.035	≤ 0.25	≤ 0.25	Bal.

Fig. 3 The macromorphology of cross section of composite coatings: (a) C1, (b) C2, (c) C3, (d) C4
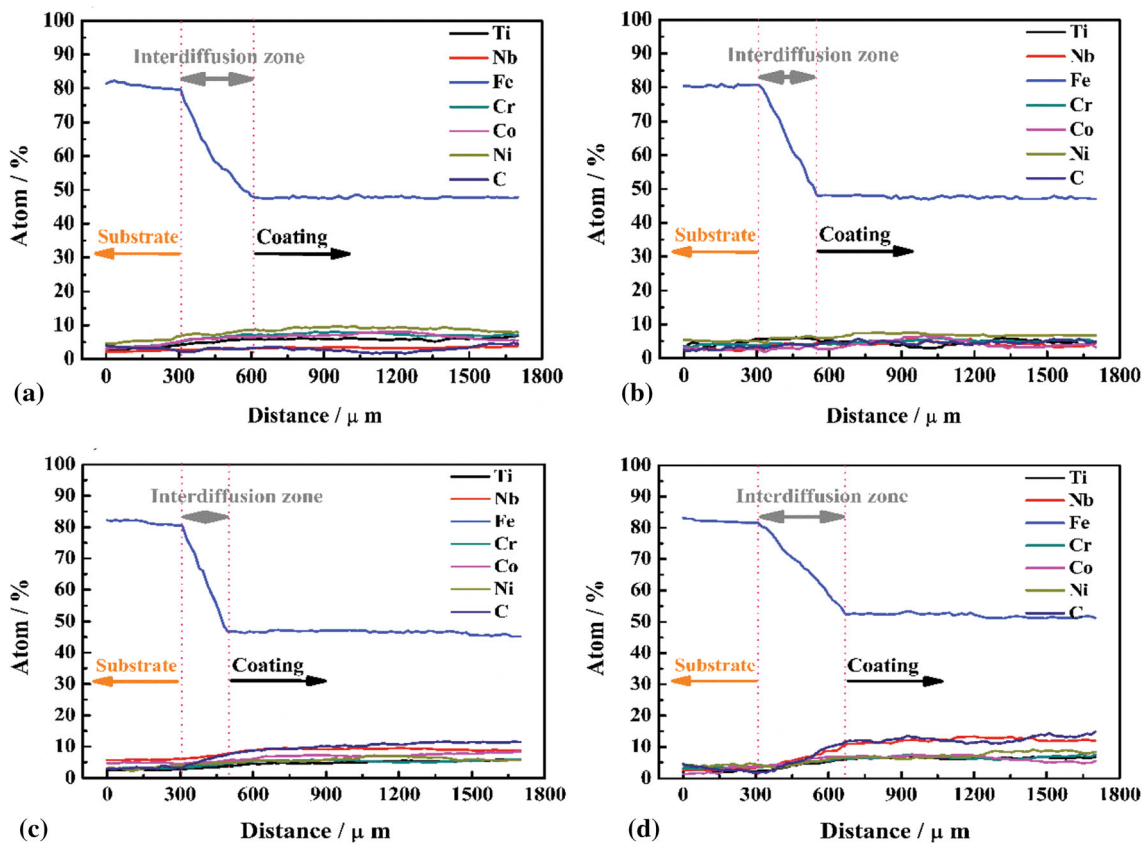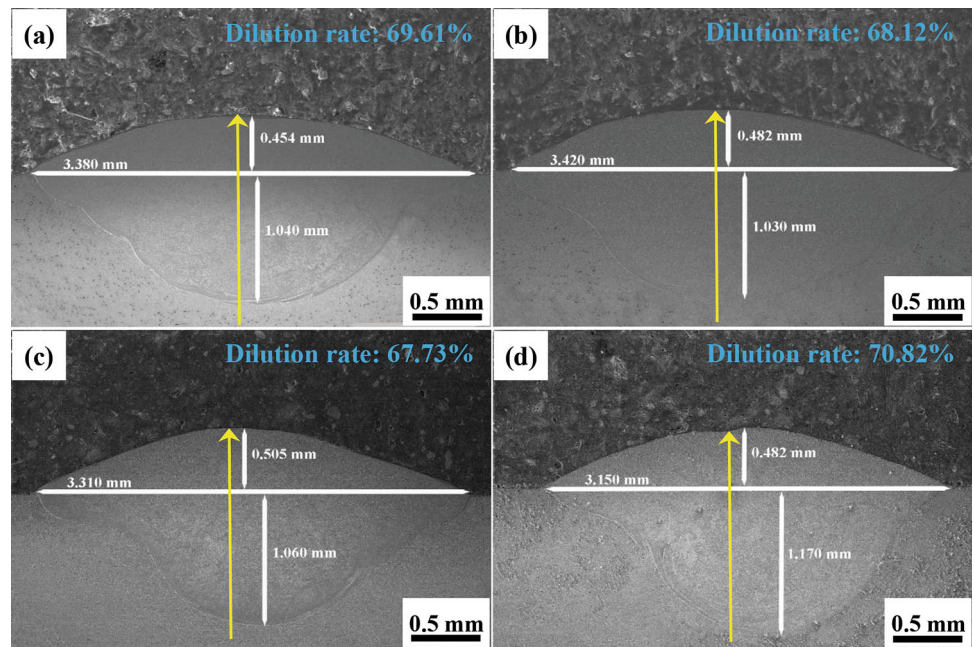
Fig. 4 The line scan results along the yellow arrow in Fig. 3: (a) C1, (b) C2, (c) C3, (d) C4
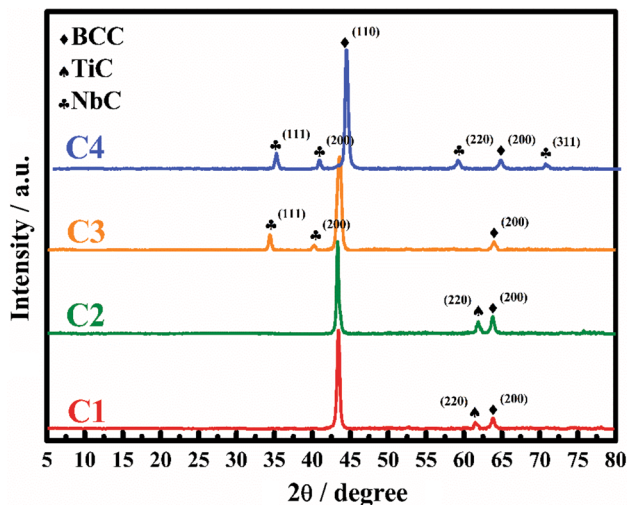
Fig. 5 The XRD patterns of composite coatings

laser energy penetrates the substrate and increases the dilution rate (Ref 27).

Phase Composition

The XRD patterns of $FeNiCoCrTi_{0.5}$-NbC_x HACCs are displayed in Fig. 5. It is clear that the composite coatings are composed of BCC solid solution and carbides. The (110) peak of the BCC solid solution is stronger than its (200) peak, implying that the BCC solid solution has a preferred orientation. In addition, the peaks of the BCC solid solution first shift slightly to the left and then shift significantly to the right with the increase of the NbC content, indicating that the lattice constant of the BCC solid solution first increases and then significantly decreases. Besides, as the NbC content increases, carbides in $FeNiCoCrTi_{0.5}$-NbC_x HACCs gradually change from TiC to NbC, which can be attributed to the diffusion and recombination of different components during cladding. In the C1 and C2, Ti atoms with kinetic advantages are quickly combined with C atoms to form TiC, whereas fewer Nb atoms are forced to squeeze into the BCC solid solution. As the NbC content increases, Nb atoms are easily combined with C atoms to form NbC (Table 3). Furthermore, a part of NbC that does not completely melt may be retained in the C3 and C4 due to the limited laser energy.

Microstructure and Chemical Composition

The microstructures of the composite coatings are exhibited in Fig. 6. It is clear that the coatings consist of matrix (1, 3, 5, 8) and precipitates (2, 4, 6, 7, 9, 10). The EDS results in Table 4 indicate that the matrix 1, 3, 5, 8 are rich in Fe, Ni, Co, and Cr as BCC solid solution corresponding

to XRD pattern. Precipitates 2 and 4 composed of Ti and C are undoubtedly determined to be TiC. Precipitates 7 and 10, whose constituent elements are mainly Nb and C, are recognized as NbC. Evidently, as the NbC content increases, carbides precipitated in the coatings are gradually transformed from TiC to NbC, which depends on the nucleation sequence that is closely related to the contents of Ti, Nb, and C. Additionally, the carbides size first decreases and then increases significantly with the increase of the NbC content, which can be ascribed to the nucleation mechanism and the precipitation behavior. Specifically, in the C1 and C2, Ti atoms with a high concentration are rapidly combined with C atoms to form TiC. In comparison with C1, the higher amount of C atoms in C2 increases the number of nucleation particles of TiC, causing a significant decrease of the TiC particle size. In the C3 and C4, the NbC content is as high as 12 wt.% and 24 wt.%, which makes Nb atoms far more than Ti atoms in the molten pool and induces the preferential nucleation of Nb and C to form NbC. Besides, Nb and C with high concentrations in C3 and C4 undergo a short-range diffusion and are strongly adsorbed on the surface of NbC, which results in a higher growth rate and a larger size. Obviously, the TiC particles in the C1 and C2 are nearly spherical, which can be ascribed to the symmetry of geometric and chemical bonds of TiC unit cells (Ref 30, 31). In the C3 and C4, Nb atoms will squeeze into TiC to destroy the stability of crystal lattice and cause the carbide to gradually evolve into multilateral granular particles. Particularly, as shown in Fig. 7(a), precipitates 6 and 9 presenting a "core–shell" structure appear in the C3 and C4 with a round black core inside and a white circle outside. The EDS results in Fig. 7(b-c7) indicate that the "core" is mainly composed of Ti, while the "shell" primarily contains Nb and C. During the cladding process, Ti-rich particles nucleate first. With the growth of Ti-rich particles, Nb and C tend to adsorb on the surface of Ti-rich particles and start heterogeneous nucleation (Ref 32) to form Ti/NbC eutectoid phase. However, these Ti/NbC eutectoid phases are not detected by XRD, which may be due to the existence of fewer Ti/NbC eutectoid phases beyond the recognition range.

Microhardness

Figure 8 displays the average microhardness and the microhardness distribution curve along the depth of cross section of $FeNiCoCrTi_{0.5}$-NbC_x HACCs. It is evident that the microhardness of the composite coatings is about twice that of the substrate. As the NbC content increases, the microhardness of $FeNiCoCrTi_{0.5}$-NbC_x does not always increase, which implies that excessive NbC is detrimental to the improvement of microhardness. As shown in Fig. 5, the peaks of the BCC solid solution first move to the left

Table 3. The values of atomic radius and the mixing enthalpy of element pairs [28, 29]

Element	Atomic radius (Å)	ΔH_{mix}, kJ mol^{-1}						
		Fe	Ni	Co	Cr	Ti	Nb	C
Fe	1.27	…	− 2	− 1	− 1	− 17	− 16	− 50
Ni	1.24		…	0	− 7	− 35	− 30	− 39
Co	1.26			…	− 4	− 28	− 25	− 42
Cr	1.28				…	− 7	− 7	− 61
Ti	1.45					…	− 2	− 109
Nb	1.48						…	− 102
C	0.86							…

Fig. 6 The representative microstructure of composite coatings: (a) C1, (b) high magnification microstructure of C1, (c) C2, (d) high magnification microstructure of C2, (e) C3, (f) high magnification microstructure of C3, (g) C4, (h) high magnification microstructure of C4
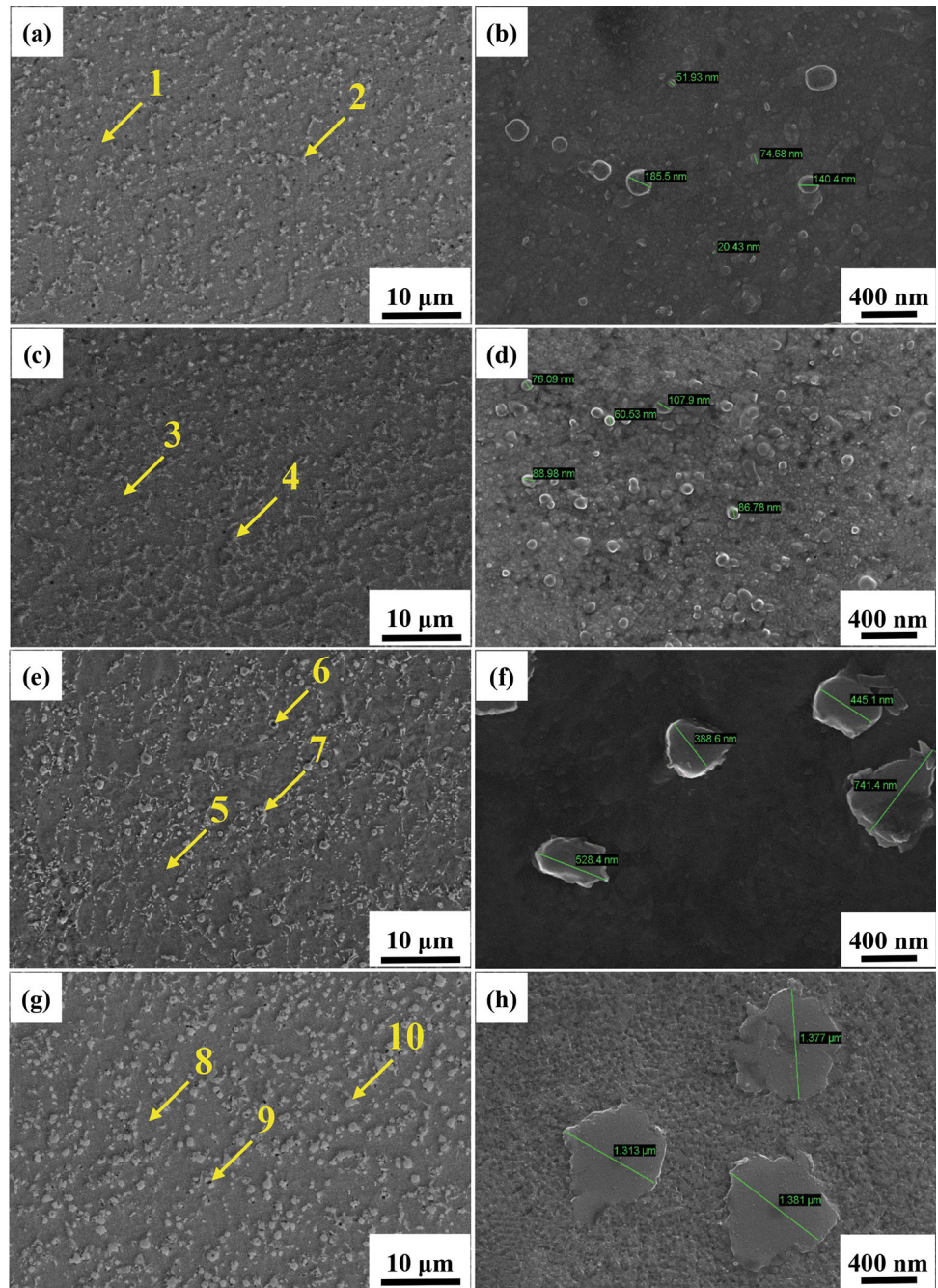
Table 4. EDS data for different phases (at.%)

Sample	Phases	Fe	Ni	Co	Cr	Ti	Nb	C
C1	1	37.99	19.51	18.70	20.88	1.17	0.66	1.09
	2	2.88	2.05	1.99	1.54	43.04	0.39	48.11
C2	3	34.63	21.57	19.12	21.34	0.83	0.79	1.72
	4	2.72	2.13	1.76	1.38	44.37	0.48	47.16
C3	5	31.12	21.83	20.02	21.46	0.62	1.71	3.24
	6	4.98	2.74	2.65	3.22	74.82	6.54	5.05
	7	3.39	1.43	1.28	2.11	1.19	46.17	44.43
C4	8	38.35	16.33	16.02	18.10	0.36	4.43	6.41
	9	4.41	1.02	1.47	1.64	78.35	7.37	5.74
	10	2.15	1.06	1.19	1.31	0.85	48.10	45.34
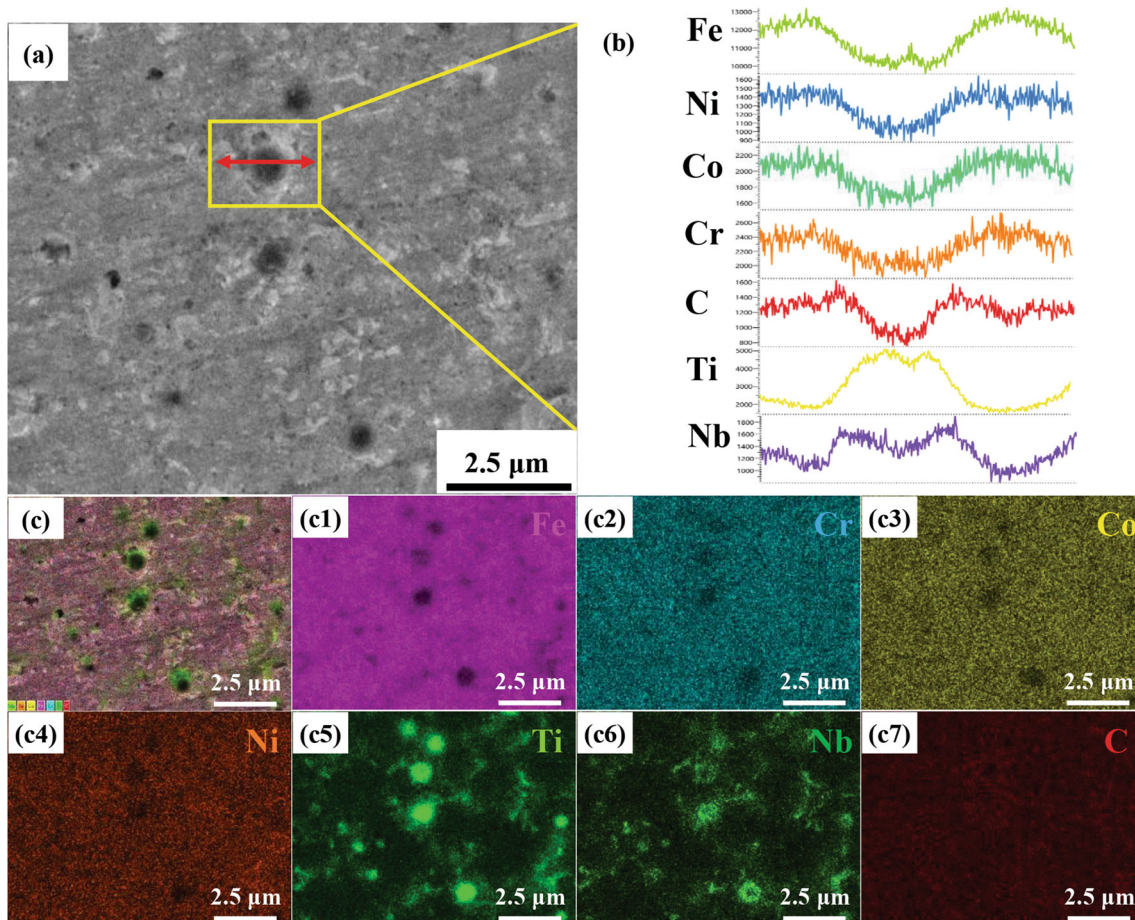
Fig. 7 The results of elemental distribution of the characteristic microstructure of C3: (a) characteristic microstructure of C3, (b) line scan results along the red arrow in (a), (c-c7) elemental distribution of the characteristic microstructure of C3

and then to the right with the increase of the NbC content, indicating that the lattice expansion of the BCC solid solution reaches saturation in the C2. For one thing, Nb atoms with a larger atomic radius squeezing into the BCC solid solution result in lattice expansion and generate an elastic stress field, which can strongly hinder dislocation slips and cause an intense displacement solid–solution strengthening effect. For another, C atoms with a smaller atomic radius occupy gaps in the BCC solid solution and aggravate the distortion of the BCC solid solution, which generates a significant interstitial solid–solution strengthening effect. Moreover, there are dispersed carbide

Fig. 8 The microhardness of composite coatings: (a) average microhardness, (b) distribution curve of microhardness
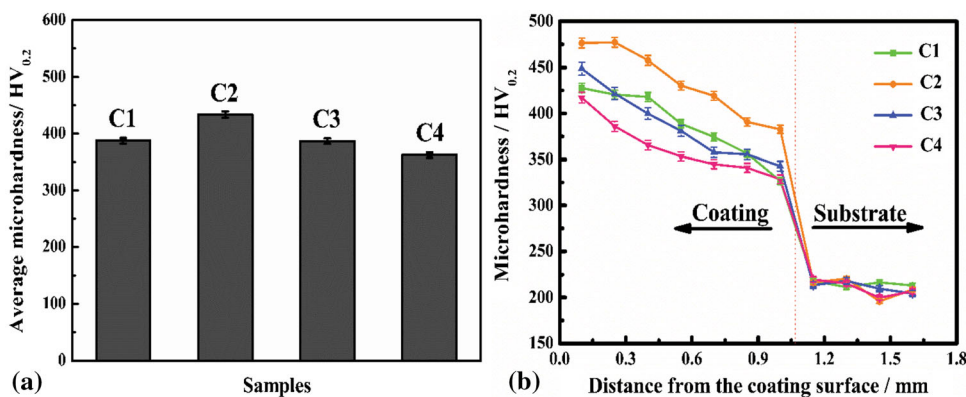
Fig. 9 The morphology of the worn surfaces: (a) C1, (b) C2, (c) C3, (d) C4
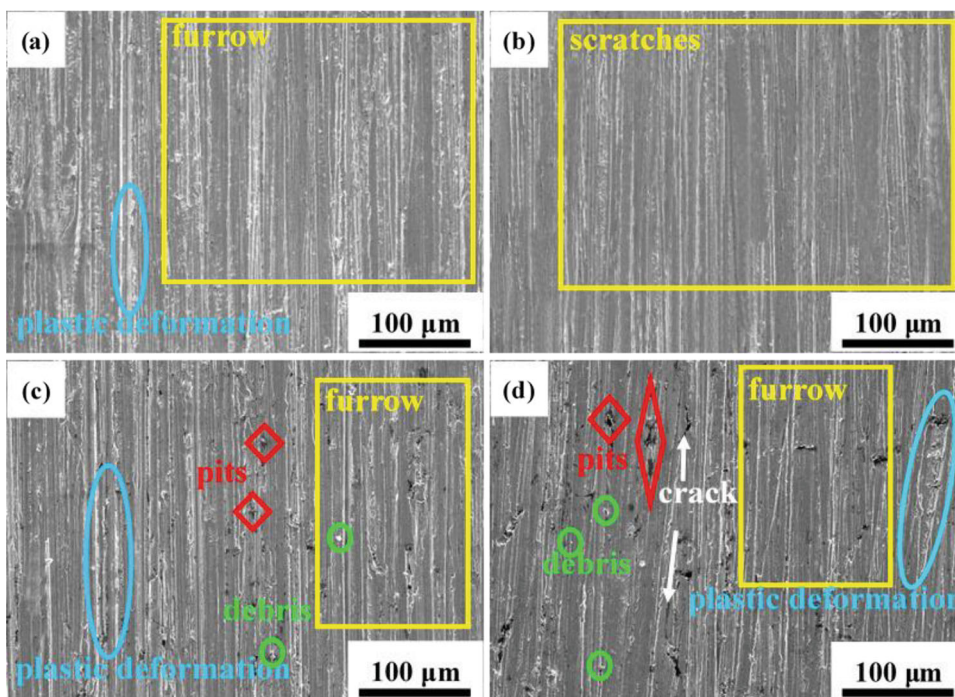
particles in the coatings that can inhibit dislocation movements and exert a second-phase strengthening effect to further enhance the microhardness. However, the strengthening effect of the second phase will decrease in the C3 and C4 with the increase of the particle size and the decrease of the number of carbide precipitates per unit area (Ref 33, 34). Especially, laser cladding with characteristics of rapid heating-solidification is conducive to obtaining fine microstructures with a high grain boundaries volume, which can make dislocation slip difficult and increase the resistance to plastic deformation.

Wear Resistance

The morphologies and two-dimensional profiles of worn surfaces of the coatings are shown in Fig. 9 and 10,

respectively. It demonstrates that abrasive wear occurs in the coatings and the wear resistance of $FeNiCoCrTi_{0.5}$-$xNbC$ HACCs first increases and then decreases with the increase of the NbC content. The deep furrows and severe plastic deformation are detected in the C1. Moreover, ridges are formed on both sides of these furrows due to the cutting of Al_2O_3 particles. As shown in Fig. 11(a-b), hard Al_2O_3 particles are embedded into micro-surface and push the surface material during the friction process when the microhardness is relatively low, which causes a certain plastic flow of the surface material and plows furrows. The C2 with high microhardness is only covered by shallow scratches due to its strong elastic deformation recovery ability that can greatly resist repeated surface plastic deformation. Compared with the C1 and C2, furrows in the C3 and C4 are significantly deeper and plastic deformation

Fig. 10 The two-dimensional profile of worn surfaces: (a) C1, (b) C2, (c) C3, (d) C4
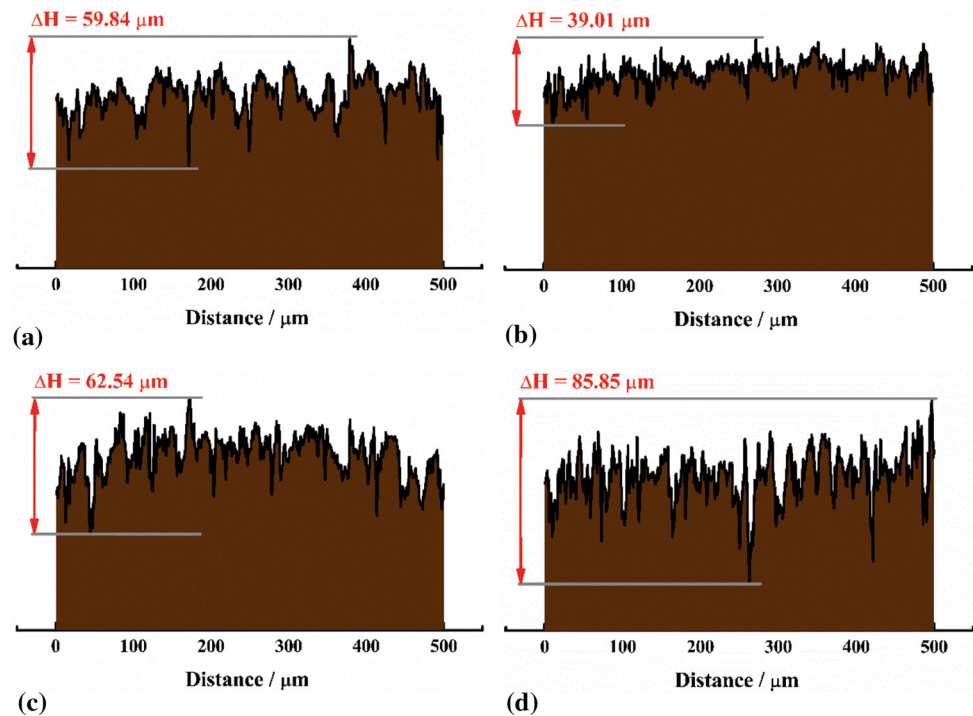
Fig. 11 The microscopic schematic diagram of friction
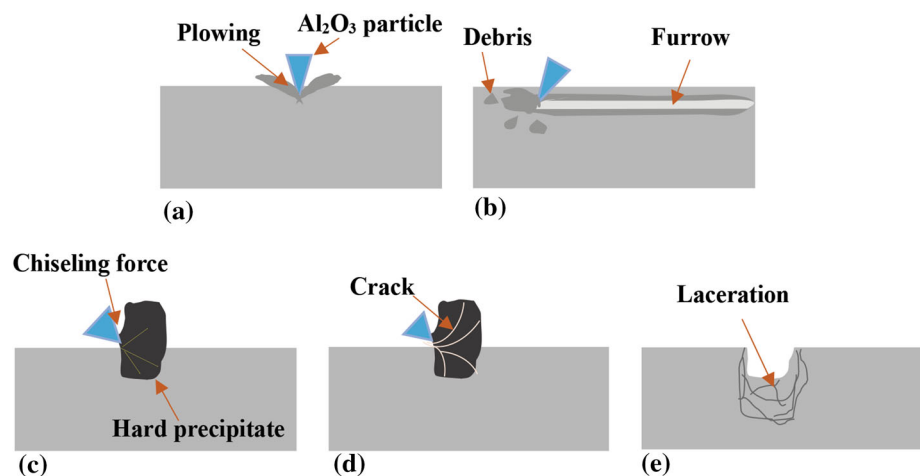
is intensified along broken particles, pits and cracks, indicating that excessive NbC can increase the brittleness of FeNiCoCrTi$_{0.5}$-xNbC HACCs (Ref 35, 36). As shown in Fig. 11(c-e), with the increase of the NbC content and the progress of the friction process, hard Al$_2$O$_3$ particles collide and mesh with bare NbC. The interaction between Al$_2$O$_3$ particles and NbC produces stress concentration at the tips of bumps on account of inhomogeneous asperity (Ref 37, 38). Moreover, hard Al$_2$O$_3$ particles dig NbC particles periodically so as to cause crack sources and microcracks. As friction progresses, tips of microcracks are torn further and cracks propagate rapidly, which leads to a gap between the matrix and NbC, inducing the

fragmentation and shedding of NbC so as to cause a certain tear to the matrix and the formation of pits. Simultaneously, a three-body friction process occurs by Al$_2$O$_3$ particles on friction pair, peeled NbC particles, and the coating to further aggravate the wear of the C3 and C4 corresponding to the wear rate in Fig. 12. Especially, the "core–shell" Ti/NbC eutectoid phase can strengthen the coatings to a certain extent. When the dislocation line bypasses the Ti/NbC eutectoid phase and the shear stress is transferred to "core", "core" Ti is more prone to distortion due to smaller elastic modulus, which improves the dislocation kinetic energy absorption ability of Ti/NbC to hinder dislocation movements and enhance the reinforcement effect

(Ref 39). The elastic modulus of the "shell" in the Ti/NbC eutectoid phase is higher than that of the "core". The elastic modulus gradient inside the Ti/NbC eutectoid phase can reduce the shear effect and decrease the crushing risk of Ti/NbC (Ref 40), so that Ti/NbC can better hinder dislocation movements and further ensure the strengthening

effect on the coatings. However, the content of the Ti/NbC eutectoid phase in the C3 and C4 is so small that it plays a limited strengthening role in the coatings. Besides, the roughness of worn surfaces of the coatings is presented in Fig. 13, which first decreases and then increases with the increase of the NbC content, implying that lower microhardness or higher brittleness will cause larger worn surface roughness. For one thing, hard Al_2O_3 particles can easily penetrate metal surface with low microhardness for severe plowing, causing ridges and wrinkles and producing high roughness. For another, brittle coating is prone to microcracks under the action of friction pair, which can cause cracking and peeling to produce high roughness.
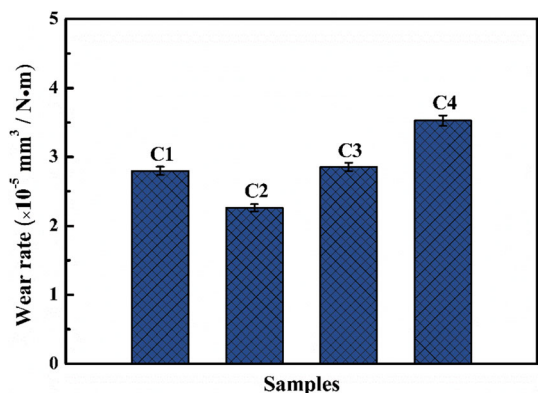
Conclusions

(1) $FeNiCoCrTi_{0.5}$-xNbC HACCs without pores, cracks and spherical adhesion are successfully prepared and metallurgically deposited on 45 steel. The dilution rate of the as-prepared composite coatings first
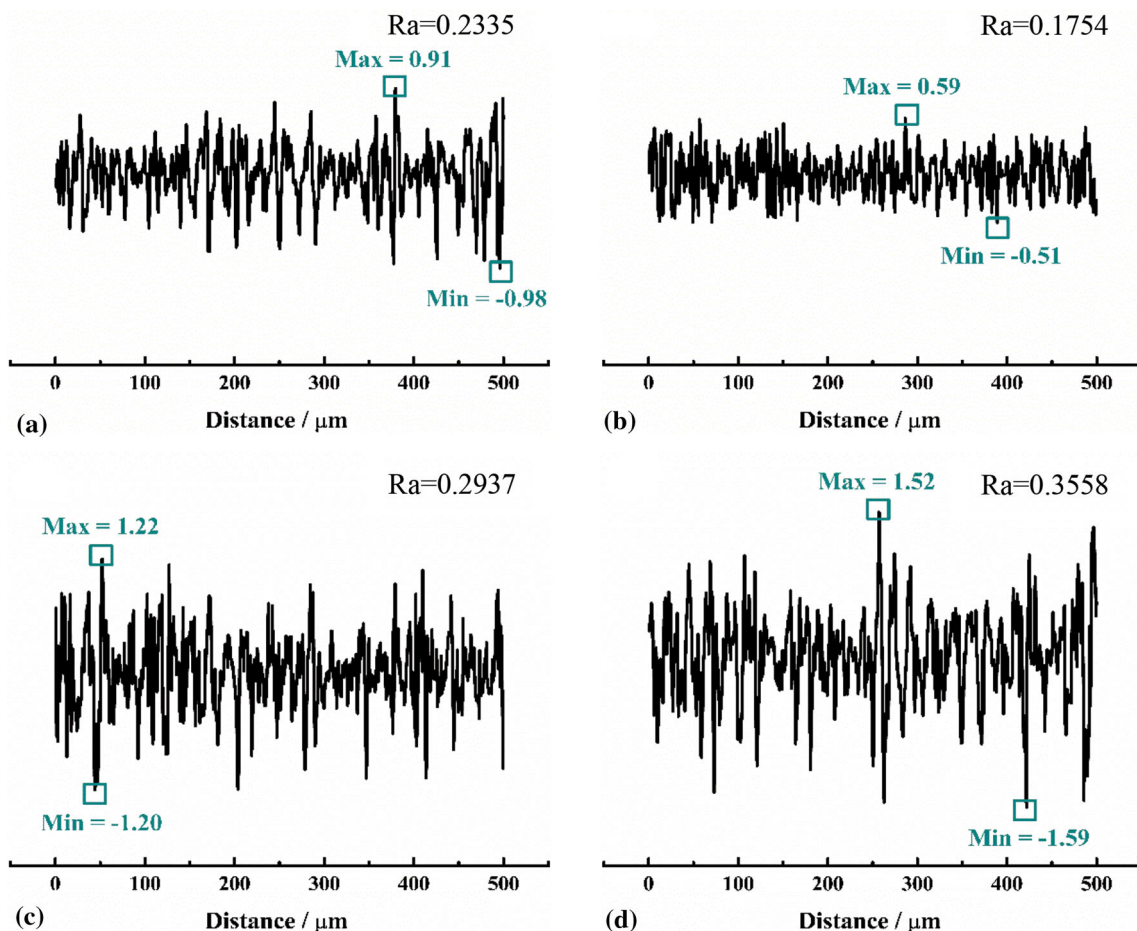
Fig. 12 The wear rate of composite coatings

Fig. 13 The roughness of worn surfaces: (a) C1, (b) C2, (c) C3, (d) C4

decreases and then increases with the increase of the NbC content.

(2) The composite coatings are mainly composed of BCC solid solution and carbides. The addition of NbC promotes the transformation of carbides from TiC to NbC, which causes the carbide morphology to change from nearly spherical to polygon with the carbide size first decreasing and then increasing significantly. The excessive NbC can induce the heterogeneous nucleation of Nb and C on the surface of Ti-rich particles to form "core–shell" Ti/NbC eutectoid phase.

(3) The microhardness of FeNiCoCrTi$_{0.5}$-xNbC HACCs is much higher than that of the substrate, which first increases and then decreases with the increase of the NbC content. The excessive NbC is not conducive to the improvement of microhardness.

(4) With the increase of the NbC content, the wear resistance of FeNiCoCrTi$_{0.5}$-xNbC HACCs first increases and then decreases. An appropriate amount of NbC can help FeNiCoCrTi$_{0.5}$-xNbC HACCs resist repeated surface plastic deformation, while excessive NbC increases the local brittleness and causes microcracks, fragmentation, spalling, and pits.

Conflict of interest No potential conflict of interest was reported by the authors.

References

1. O. Trunova, T. Beck, R. Herzog, R.W. Steinbrech and L. Singheiser, Damage Mechanisms and Lifetime Behavior of Plasma Sprayed Thermal Barrier Coating Systems for Gas Turbines-Part I: Experiments, *Surf. Coat. Technol.*, 2008, **202**(20), p 5027–5032.

2. Y.Q. Wang and G. Sayre, Commercial Thermal Barrier Coatings with a Double-Layer Bond Coat on Turbine Vanes and the Process Repeatability, *Surf. Coat. Technol.*, 2009, **203**(16), p 2186–2192.

3. J.W. Yeh, S.K. Chen, S.J. Lin, J.Y. Gan, T.S. Chin, T.T. Shun, C.H. Tsau and S.Y. Chang, Nanostructured High-Entropy Alloys with Multiple Principal Elements: Novel Alloy Design Concepts and Outcomes, *Adv. Eng. Mater.*, 2004, **6**(5), p 299–303.

4. J.W. Yeh, S.J. Lin, T.S. Chin, J.Y. Gan, S.K. Chen, T.T. Shun, C.H. Tsau and S.Y. Chou, Formation of Simple Crystal Structures in Solid-Solution Alloys with Multi-Principal Metallic Elements, *Metall. Mater. Trans. A*, 2004, **35**, p 2533–2536.

5. S. Fida Hassan, G.J. Nadhreen, M.A.A. Al-Jeddawi and M. Al-Otaibi, Effect of Powder Processing on Microstructure and Mechanical Properties of a High-Entropy Al$_{24.2}$Si$_{3.2}$Cu$_{24.2}$Ti$_{24.2}$Ni$_{24.2}$ Alloy, *Philos. Mag. Lett.*, 2020, **100**(4), p 171–180.

6. W.R. Wang, W. Qi, X.L. Zhang, X. Yang, L. Xie, D.Y. Li and Y.H. Xiang, Superior Corrosion Resistance-Dependent Laser Energy Density in (CoCrFeNi)$_{95}$Nb$_5$ High Entropy Alloy Coating Fabricated by Laser Cladding, *Int. J. Min. Met. Mater.*, 2021, **28**, p 888–897.

7. S.H. Kuang, F. Zhou, S.S. Zheng and Q.B. Liu, Annealing-Induced Microstructure and Properties Evolution of Refractory MoFeCrTiWAlNb$_3$ Eutectic High-Entropy Alloy Coating by Laser Cladding, *Intermetallics*, 2021, **129**, p 107039.

8. C. Chen, N. Liu, J. Zhang, J. Cao, L.J. Wang and H.F. Xiang, Microstructure Stability and Oxidation Behaviour of (FeCoNiMo)$_{90}$(Al/Cr)$_{10}$ High-Entropy Alloys, *Mater. Sci. Technol.-Lond*, 2019, **35**(15), p 1883–1890.

9. J. Wang, Z. Zheng, J. Xu and Y. Wang, Microstructure and Magnetic Properties of Mechanically Alloyed FeSiBAlNi (Nb) High Entropy Alloys, *J. Magn. Magn. Mater.*, 2014, **355**, p 58–64.

10 L. Zendejas Medina, L. Riekehr and U. Jansson, Phase Formation in Magnetron Sputtered CrMnFeCoNi High Entropy Alloy, *Surf. Coat. Technol.*, 2020, **403**, p 126323.

11. Y. Zhang, T.F. Han, M. Xiao and Y.F. Shen, Effect of iron content on microstructure and properties of Fe$_x$Ni$_2$Co$_2$CrTiNb high-entropy alloy coating, *Optik*, 2020, **204**, p 164168.

12. C.L. Chen and Suprianto, Microstructure and Mechanical Properties of AlCuNiFeCr High Entropy Alloy Coatings by Mechanical Alloying, *Surf. Coat. Technol.*, 2020, **386**, p 125443

13. Y. Ma, G.J. Peng, D.H. Wen and T.H. Zhang, Nanoindentation Creep Behavior in a CoCrFeCuNi High-Entropy Alloy Film with Two Different Structure States, *Mater. Sci. Eng. A*, 2015, **621**, p 111–117.

14. S. Zanzarin, S. Bengtsson and A. Molinari, Study of Dilution in Laser Cladding of a Carbon Steel Substrate with Co Alloy Powders, *Powder Metall.*, 2016, **59**(1), p 85–94.

15. E.M. Stanciu, A. Pascu, M.H. Țierean, I. Voiculescu, I.C. Roată, C. Croitoru and I. Hulka, Dual Coating Laser Cladding of NiCrBSi and Inconel 718, *Mater. Manuf. Process.*, 2016, **31**(12), p 1556–1564.

16. N.V. Kobernik, R.S. Mikheev, M. Brzhezinskaya and N.P. Aleshin, Effect of Carbon Nanotubes on Structure and Properties of the Antifriction Coatings Produced by Plasma Cladding, *Fuller. Nanotubes Carbon Nanostruct.*, 2020, **28**(7), p 515–520.

17. F.Y. Shu, B. Wang, H.Y. Zhao, C.W. Tan, J.L. Zhou and J. Zhang, Effects of Line Energy on Microstructure and Mechanical Properties of CoCrFeNiBSi High-Entropy Alloy Laser Cladding Coatings, *J. Therm. Spray Technol.*, 2020, **29**(4), p 789–797.

18. H.F. Zhuang, Q. Zhang and D.L. Zhang, Microstructure and Tribological Properties of Ni-Based Laser-Clad Coatings by Rare Earth Modification, *J. Therm. Spray Technol.*, 2021 https://doi.org/10.1007/s11666-021-01193-z

19. X.W. Qiu and C.G. Liu, Microstructure and Properties of Al$_2$CrFeCoCuTiNi$_x$ High Entropy Alloys Prepared by Laser Cladding, *J. Alloy Compd.*, 2013, **553**, p 216–220.

20. Q.H. Fang, Y. Chen, J. Li, Y.B. Liu and Y. Liu, Microstructure and Mechanical Properties of FeCoCrNiNb$_x$ High Entropy Alloy Coatings, *Physica B*, 2018, **550**, p 112–116.

21. X.W. Qiu, Microstructure and Mechanical Properties of CoCrFeNiMo High-Entropy Alloy Coatings, *J. Mater. Res. Technol.*, 2020, **9**(3), p 5127–5133.

22. D. Lin, N. Zhang, B. He, X. Gong, Y. Zhang, D. Li and F. Dong, Structural Evolution and Performance Changes in FeCoCrNiAlNb$_x$ High-Entropy Alloy Coatings Cladded by Laser, *J. Therm. Spray Technol.*, 2017, **26**(8), p 1–8.

23. R. Abramowitz and S.H. Yalkowsky, Melting Point, Boiling Point, and Symmetry, *Pharm. Res-dordr*, 1990, **7**(9), p 942–947.

24. H.F. Liu, H.J. Su, Z.L. Shen, D. Zhao, Y. Liu, M. Guo, Y.L. Guo, J. Zhang, L. Liu and H.Z. Fu, Effect of Scanning Speed on the

Solidification Process of Al_2O_3/$GdAlO_3$/ZrO_2 Eutectic Ceramics in a Single Track by Selective Laser Melting, *Ceram. Int.*, 2019, **45**(14), p 17252–17257.

25. J. Zou, Y. Gaber, G. Voulazeris, S. Li, L. Vazquez, L.F. Liu, M.Y. Yao, Y.J. Wang, M. Holynski, K. Bongs and M.M. Attallah, Controlling the Grain Orientation During Laser Powder Bed Fusion to Tailor The Magnetic Characteristics in a Ni-Fe Based Soft Magnet, *Acta Mater.*, 2018, **158**, p 230–238.

26. Y. Li, J. Yao and Y. Liu, Synthesis and Cladding of Al_2O_3 Ceramic Coatings on Steel Substrates by a Laser Controlled Thermite Reaction, *Surf. Coat. Technol.*, 2003, **172**(1), p 57–64.

27. K.F. Dang and Z.Q. Jiang, Microstructure Evolution and Properties of a Laser Cladded Ni-Based WC Reinforced Composite Coating, *Mater. Test.*, 2020, **62**(11), p 1078–1084.

28. L. Pauling, Atomic radii and interatomic distances in metals, *J Am Chem Soc*, 1947, **69**(3), p 542–553.

29. A. Takeuchi and A. Inoue, Calculations of Mixing Enthalpy and Mismatch Entropy for Ternary Amorphous Alloys, *Mater. Trans.*, 2000, **41**(11), p 1372–1378.

30. X.D. Sun, H.G. Zhu, J.L. Li, J.W. Huang and Z.H. Xie, High Entropy Alloy FeCoNiCu Matrix Composites Reinforced with in-situ TiC Particles and Graphite Whiskers, *Mater. Chem. Phys.*, 2018, **220**, p 449–459.

31. J. Joseph, N. Haghdadi, K. Shamlaye, P. Hodgson, M. Barnett and D. Fabijanic, The Sliding Wear Behaviour of CoCrFeMnNi and Al_xCoCrFeNi High Entropy Alloys at Elevated Temperatures, *Wear*, 2019, **428–429**, p 32–44.

32. K.F. Kelton and A.L. Greer, Nucleation in Condensed Matter: Applications in Materials and Biology, *Pergamon Mater. Ser.*, 2010, **15**, p 587–622.

33. S.W. Park, C. Park, Y.S. Na, H.S. Kim and N. Kang, Effects of (W, Cr) Carbide on Grain Refinement and Mechanical Properties for CoCrFeMnNi High Entropy Alloys, *J. Alloy Compd.*, 2019, **770**, p 222–228.

34. Q.T. Li, Y.P. Lei and H.G. Fu, Growth Characteristics and Reinforcing Behavior of in-situ NbCp in Laser Cladded Fe-Based Composite Coating, *J. Mater. Sci. Technol.*, 2015, **31**(7), p 766–772.

35. D.Y. Lin, N.N. Zhang, B. He, G.W. Zhang, Y. Zhang and D.Y. Li, Tribological Properties of $FeCoCrNiAlB_x$ High-Entropy Alloys Coating Prepared by Laser Cladding, *J. Iron Steel Res. Int.*, 2017, **24**(2), p 184–189.

36. X.F. Li, Y.H. Feng, B. Liu, D.H. Yi, X.H. Yang, W.D. Zhang, G. Chen, Y. Liu and P.K. Bai, Influence of NbC Particles on Microstructure and Mechanical Properties of AlCoCrFeNi High-Entropy Alloy Coatings Prepared by Laser Cladding, *J. Alloy Compd.*, 2019, **788**, p 485–494.

37. N.N. Zhao, Y.H. Xu, X. Huang, L.S. Zhong and J.L. Lu, Microstructure and Wear Properties of Niobium Carbide Particulates Gradient-Distribution Composite Layer Fabricated In Situ, *Ceram. Int.*, 2016, **42**(16), p 18507–18515.

38. V.L. Arantes, L.M. Genova, P.H.B.P. Guimaraes, C.A. Fortulan and J. Vleugels, Influence of NbC Content on the Wear Resistance of Alumina/Niobium Carbide Tools, *Mater. Res.*, 2021, **24**(4), p e20200552.

39. L.E. Popov, S.N. Kolupaeva, N.A. Vikhor' and S.I. Puspesheva, Dislocation Dynamics of Crystallographic Slip, *Russ. Phys. J.*, 2000, **43**, p 66–70.

40. J. Malzbender, The Use of Theories to Determine Mechanical and Thermal Stresses in Monolithic, Coated and Multilayered Materials with Stress-Dependent Elastic Modulus or Gradient in Elastic Modulus Exemplified for Thermal Barrier Coatings, *Surf. Coat. Techno.*, 2004, **186**(3), p 416–422.